





RESEARCH ARTICLE | OCTOBER 09 2023

Berry curvature induced spontaneous and topological-like Hall effect in magnetic Weyl semimetallic $\text{Nd}_2\text{Ir}_2\text{O}_7$ (111) thin films


Mithun Ghosh  ; P. D. Babu  ; P. S. Anil Kumar  



APL Mater. 11, 101109 (2023)
<https://doi.org/10.1063/5.0166455>




CrossMark



Physics of Fluids

Special Topic: K. R. Sreenivasan:
A Tribute on the occasion of his 75th Birthday

Submit Today



Berry curvature induced spontaneous and topological-like Hall effect in magnetic Weyl semimetallic $\text{Nd}_2\text{Ir}_2\text{O}_7$ (111) thin films

Cite as: APL Mater. 11, 101109 (2023); doi: 10.1063/5.0166455
 Submitted: 5 July 2023 • Accepted: 25 September 2023 •
 Published Online: 9 October 2023



Mithun Ghosh,¹ P. D. Babu,² and P. S. Anil Kumar^{1,a)}

AFFILIATIONS

¹Department of Physics, Indian Institute of Science, Bangalore 560012, Karnataka, India

²UGC-DAE Consortium for Scientific Research, 246-C, CFB, BARC Campus, Mumbai 400085, India

^{a)}Author to whom correspondence should be addressed: anil@iisc.ac.in

ABSTRACT

We report a study of longitudinal resistivity, anisotropic magnetoresistance (MR), and Hall effect on epitaxial $\text{Nd}_2\text{Ir}_2\text{O}_7$ (111) thin films grown by the solid phase epitaxy technique, in which spin-orbit coupling, electronic correlation, magnetic frustration, and f - d exchange interaction are present. Temperature-dependent longitudinal resistivity (ρ_{xx}) data indicate semimetallic charge transport in the low-temperature region. Field-cooled longitudinal resistivity measurements detect negligible domain-wall conductance compared to the polycrystal or single-crystal samples. Angle-dependent MR measurement shows that the magnetic structure of Ir^{4+} $5d$ moments can be finely tuned by applying a magnetic field along different crystallographic directions. MR measurements show a field-induced modification of the Nd^{3+} $4f$ spin structure from all-in-all-out/all-out-all-in (AIAO/AOAI) (4-in-0-out) to 1-in-3-out for the applied field (H) along the [111] direction, resulting in field-induced plastic deformation of the Ir^{4+} domain distribution. In contrast, the application of field (H) along the [001] and [011] directions could not modify any domain distribution. A large spontaneous Hall effect (SHE) signal has been observed on $\text{Nd}_2\text{Ir}_2\text{O}_7$ (111) thin film with AIAO/AOAI antiferromagnetic ordering for the application of field (H) along [001], $[\bar{1}\bar{1}0]$, and [111] directions. The appearance of a large spontaneous Hall signal for the applied field along [001] and $[\bar{1}\bar{1}0]$ directions rules out domain switching as the origin of the Hall effect and confirms the presence of the Weyl semimetallic phase in $\text{Nd}_2\text{Ir}_2\text{O}_7$ (111) thin films. In addition to SHE, a large topological-like Hall signal is also observed, possibly due to the presence of multiple Weyl nodes in the electronic band structure.

© 2023 Author(s). All article content, except where otherwise noted, is licensed under a Creative Commons Attribution (CC BY) license (<http://creativecommons.org/licenses/by/4.0/>). <https://doi.org/10.1063/5.0166455>

I. INTRODUCTION

Since the theoretical prediction of Weyl Fermions in the low-energy excitation of antiferromagnetic (AFM) $\text{Y}_2\text{Ir}_2\text{O}_7$,¹ the rare-earth (RE) pyrochlore iridate ($RE_2\text{Ir}_2\text{O}_7$) family has attained considerable interest.^{2–4} The magnetic structure of pyrochlore iridates $RE_2\text{Ir}_2\text{O}_7$ is known to possess a highly geometrically frustrated lattice that is composed of two magnetic sublattices of RE^{3+} and Ir^{4+} sites. These sublattices are structurally identical but are displaced by half a lattice constant from each other along the [111] direction of the unit cell.⁵ In each sublattice, the ions form an infinite network of corner-sharing tetrahedra. This connectivity between the magnetic sites gives rise to frustration, and a number of magnetic ground states are predicted to exist.^{1,6} Among them, $\text{Nd}_2\text{Ir}_2\text{O}_7$ is of

particular interest because of its electronic ground state that lies on the boundary of the metal-insulator transition.^{7,8}

In the case of $\text{Nd}_2\text{Ir}_2\text{O}_7$, the Nd^{3+} $4f$ localized moments are constrained by easy-axis anisotropy to point either into or out of each tetrahedron (i.e., parallel or anti-parallel to the local [111] axis). On the other hand, due to the presence of finite octahedral crystal field splitting (Δ) and spin-orbit coupling (λ), the Ir^{4+} $5d$ itinerant electrons carry a $J_{\text{eff}} = 1/2$ effective pseudospin and orders in an all-in-all-out/all-out-all-in (AIAO/AOAI) type antiferromagnetic (AFM) structure [shown in Fig. 3(c)] by the nearest-neighbor AFM exchange coupling, below its ordering temperature T_N .⁷ The localized Nd^{3+} $4f$ moments interact with the Ir^{4+} $5d$ itinerant electrons through f - d exchange interaction and give rise to AIAO/AOAI AFM order below $T_{\text{Nd}} \sim 15 \pm 5$ K.^{9,10} Therefore, the strength of the f - d

exchange interaction appears to be $J_{fd} \sim 15 \pm 5$ K. In the presence of f - d exchange interactions, the Weyl semimetal (WSM) phase is predicted to stabilize over a larger parameter space than that induced by the d -electron correlations alone.¹¹

Naturally, an open question arises about the influence of the Nd^{3+} moments on the Ir^{4+} spin structure. It is well known that the Nd^{3+} moments ($\sim 2.4 \mu_B/\text{Nd}$) are much larger than the Ir^{4+} moments ($\sim 0.2 \mu_B/\text{Ir}$).¹² Therefore, the effect of the external magnetic field on the Ir^{4+} moments could be amplified by the large Zeeman energy of the Nd^{3+} moments and the associated f - d exchange interaction.^{12–14} In correlated electron systems, the modified spin structure will affect the charge dynamics and is expected to cause unconventional magnetotransport phenomena.^{15,16} Here, we used this approach and tried to asymmetrically modify the Ir^{4+} domain distribution (proportion of A and B domains) by the applied magnetic field along different crystallographic directions and consequently studied the magnetotransport phenomena.

Besides the non-coplanar geometrically frustrated magnetic structure of $\text{Nd}_2\text{Ir}_2\text{O}_7$, its electronic band structure also generated considerable interest, like magnetic Weyl semimetal (WSM),^{17,18} large anomalous domain wall (DW) conductance,^{19,20} and field-induced insulator-semimetal transition.^{12,13} The low-temperature optical conductivity study by Udea *et al.* on polycrystalline $\text{Nd}_2\text{Ir}_2\text{O}_7$ has confirmed the presence of a charge gap of 45 meV.^{21,22} On the other hand, the transport study by Disseler *et al.* on polycrystalline $\text{Nd}_2\text{Ir}_2\text{O}_7$ reveals the absence of any metal-insulator transition.²³ Although Yanagishima and Maeno show metallic conductivity without any indication of magnetic ordering of Ir^{4+} moments.²⁴ These observations suggest widely different ground states in $\text{Nd}_2\text{Ir}_2\text{O}_7$, from charge-gaped insulators to zero gap semimetals or metals, which might arise due to slight Nd/Ir off-stoichiometry in $\text{Nd}_2\text{Ir}_2\text{O}_7$, like other pyrochlore iridates.^{25–27} A recent study by Kim *et al.* on $\text{Nd}_2\text{Ir}_2\text{O}_7$ (111) thin films indicates semimetallic charge transport down to the lowest measured temperature of 2 K.¹⁷ Furthermore, a single crystal study by Udea *et al.* on $\text{Nd}_2\text{Ir}_2\text{O}_7$ under an applied hydrostatic pressure shows stabilization of the WSM phase within a few Kelvin of the temperature region just below the AIAI/AOAI AFM ordering temperature T_N .¹⁸ The above-mentioned observations imply that below T_N , the AFM ordering of Ir^{4+} can stabilize topological electronic phases with a number of Weyl nodes in momentum space. The Weyl nodes behave as a source or sink of Berry phase curvature in momentum space and can induce a large intrinsic anomalous Hall effect (AHE). Previous theoretical calculations on pyrochlore iridates have predicted the emergence of an anomalous Hall conductance (AHC) for applied pressure along the [111] direction²⁸ or a (111) oriented grown thin film²⁹ whose value is proportional to the separation of Weyl nodes in momentum space, $\sigma_{xy}^{\text{AHC}} = (e^2/h)(2k_0/2\pi)$, where $2k_0$ is the separation between two Weyl points (WPs). Therefore, in the WSM, the AHC (σ_{xy}^{AHC}) will interestingly reflect the position of the WPs in the Brillouin zone (BZ). When the WPs are moved to the BZ boundary and two WPs with opposite chirality meet and are annihilated, the system can become a quantized 3D anomalous Hall state.^{29,30}

This signifies that the single-crystalline thin film of the correlated topological material $\text{Nd}_2\text{Ir}_2\text{O}_7$ will be a new platform for exploring novel topological phenomena in momentum space. For the understanding of the spin structure as well as the electronic band

structure, here we have investigated detailed and comprehensive magnetotransport properties of epitaxial $\text{Nd}_2\text{Ir}_2\text{O}_7$ (111) thin films grown on YSZ(111) substrate, down to 2 K and up to ± 140 kOe of the magnetic field. For the investigation of unconventional DW conductance, longitudinal resistivity (ρ_{xx}) measurements were carried out on untrained and trained ($+140$ kOe FC) samples, respectively. The electronic structure of $\text{Nd}_2\text{Ir}_2\text{O}_7$ is close to WSM and causes a large intrinsic anomalous Hall effect, and a large topological-like Hall signal appears, possibly due to the presence of multiple Weyl nodes.

II. EXPERIMENTAL DETAILS

In this present study, we use $\text{Nd}_2\text{Ir}_2\text{O}_7$ thin film grown on a 3×3 mm² YSZ(111) substrate using a pulsed laser deposition (PLD) system, followed by *ex-situ* air annealing. Before the PLD process, the commercially bought YSZ (111) substrates were air annealed at 1250 °C for 2 h in order to get an atomically smooth step and terrace structured substrate surface (data are shown in supplementary material).³⁰ The sample fabrication protocol is kept the same as in the earlier report.²⁷ The crystallinity of post-annealed $\text{Nd}_2\text{Ir}_2\text{O}_7$ thin films was characterized using a Rigaku SmartLab high-resolution four-circle x-ray diffractometer (XRD) with Cu- $K_{\alpha 1}$ radiation. The electrical and magnetotransport properties were measured in Dyna-Cool physical property measurement systems (PPMS) (Resistivity option, Quantum Designs) on a Hall bar by the four-probe method. To give electrical contact, Al (25 μm diameter) wire is bonded to the sample by ultrasonic vibration using the TPT wire bonding tool.

III. RESULTS AND DISCUSSION

A. Structural analysis of $\text{Nd}_2\text{Ir}_2\text{O}_7$ (111) thin film

Figure 1(a) shows the XRD θ - 2θ pattern of post-annealed $\text{Nd}_2\text{Ir}_2\text{O}_7$ thin films grown on the YSZ(111) substrate. It can be seen that only (111) oriented well-defined sharp peaks of $\text{Nd}_2\text{Ir}_2\text{O}_7$ are present. The presence of odd-numbered peaks is a good conformation of phase pure pyrochlore structure (within our experimental limit). Though the $\text{Nd}_2\text{Ir}_2\text{O}_7$ peaks appeared symmetric, the possibility of defects such as vacancies, dislocation, and micro-crystalline strain in the film cannot be completely ruled out. From the out-of-plane XRD measurement, the out-of-plane lattice parameter d_{111} appeared to be $\sim 6.00(2)$ Å. To check the mosaic spread of the single crystalline sample, a rocking curve around the $\text{Nd}_2\text{Ir}_2\text{O}_7$ (222) peak is performed and plotted in Fig. 1(b). The black open circles represent the experimental data, and the solid red line corresponds to the pseudo-Voigt fitting of the data, which yields FWHM as 0.10° . The low value of FWHM corresponds to the high quality of the samples. To verify the strained or relaxed growth of $\text{Nd}_2\text{Ir}_2\text{O}_7$ on YSZ, an asymmetric reciprocal space mapping (RSM) around the YSZ(331) and $\text{Nd}_2\text{Ir}_2\text{O}_7$ (662) peak is performed and plotted in Fig. 1(c). The high and low intensity (marked by a red star) peaks correspond to the YSZ(331) and $\text{Nd}_2\text{Ir}_2\text{O}_7$ (662) planes, respectively. It can be seen that the YSZ(331) and $\text{Nd}_2\text{Ir}_2\text{O}_7$ (662) peaks are well separated from each other. The position of the $\text{Nd}_2\text{Ir}_2\text{O}_7$ (662) peaks corresponds mostly to the relaxed growth of $\text{Nd}_2\text{Ir}_2\text{O}_7$ on the YSZ(111) substrate. In order to check the epitaxial relationship between the thin film and the substrate, an azimuthal ϕ scan

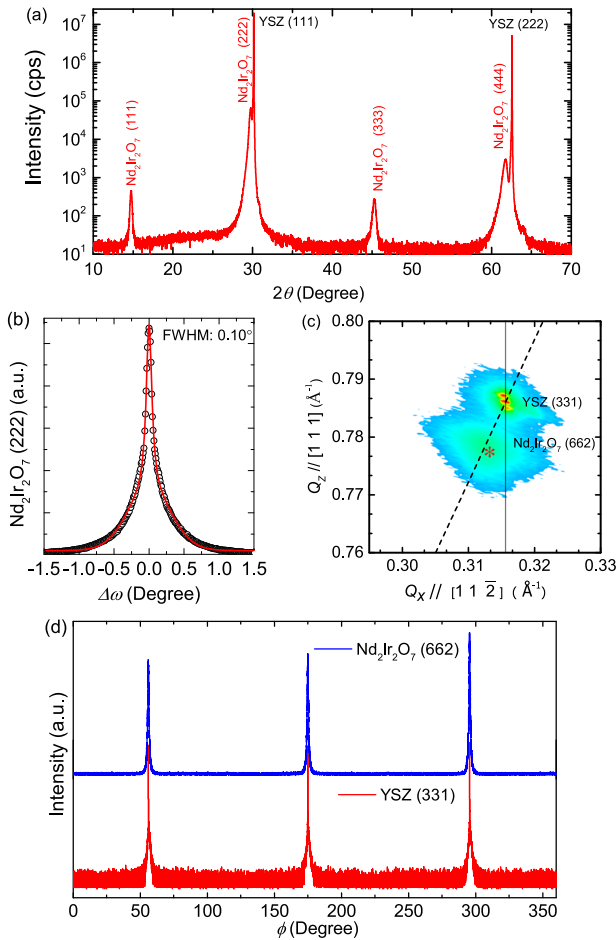


FIG. 1. (a) XRD θ - 2θ pattern of post-annealed $\text{Nd}_2\text{Ir}_2\text{O}_7$ thin film having thickness ~ 60 nm, grown on (111) oriented YSZ substrate. (b) Rocking curve measurement of $\text{Nd}_2\text{Ir}_2\text{O}_7$ around the (222) peak. (c) Asymmetric reciprocal space mapping around YSZ(331) and $\text{Nd}_2\text{Ir}_2\text{O}_7$ (662) peaks. The vertical solid line corresponds to coherent growth, whereas the dashed line passing through the origin of the Q_x - Q_z plot is the guide for relaxed cubic growth. (d) Azimuthal ϕ scan around YSZ(331) (red line) and $\text{Nd}_2\text{Ir}_2\text{O}_7$ (662) peak (blue line).

has been performed around YSZ(331) and $\text{Nd}_2\text{Ir}_2\text{O}_7$ (662) peaks and plotted in Fig. 1(d). For both the $\text{Nd}_2\text{Ir}_2\text{O}_7$ (662) (blue line) and YSZ(331) (red line) planes, three equally spaced peaks appeared, which corresponds to the presence of three-fold cubic symmetry in $\text{Nd}_2\text{Ir}_2\text{O}_7$ as well as in YSZ. For both the sample and substrate, the peaks appear on the same ϕ value, implying no in-plane rotation of the film with respect to the substrate and thus indicating a good epitaxial growth of $\text{Nd}_2\text{Ir}_2\text{O}_7$ on YSZ(111). It implies a cube-on-cube epitaxial growth of $\text{Nd}_2\text{Ir}_2\text{O}_7$ with the following epitaxial relation: $(222)[222] \text{Nd}_2\text{Ir}_2\text{O}_7 \parallel (111)[111] \text{YSZ}$ and $(224)[22\bar{4}] \text{Nd}_2\text{Ir}_2\text{O}_7 \parallel (11\bar{2})[11\bar{2}] \text{YSZ}$.

B. Longitudinal resistivity of $\text{Nd}_2\text{Ir}_2\text{O}_7$

The temperature dependence of longitudinal resistivity ρ_{xx} (red curve) and the corresponding temperature derivative (blue curve)

have been plotted in Fig. 2(a). It is observed that as the temperature decreases from 300 K, the resistivity sharply decreases and exhibits a broad minimum around 55 K, which corresponds to metallic charge transport in the high-temperature region (55–300 K), below which it increases as temperature decreases. The transition from metallic to non-metallic behavior around 55 K is associated with the Ir^{4+} AIAO/AOAI AFM ordering.^{10,31} Below 55 K, the resistivity increases weakly as the temperature decreases to 20 K. However, there is a second slope change around 20 K [this feature is more clear in Fig. 2(b), where the temperature is plotted on a log scale], and the resistivity increases sharply as the temperature lowers down to 2 K. The transition at 20 K is most likely associated with the all-in-all-out/all-out-all-in (AIAO/AOAI) antiferromagnetic (AFM) ordering of Nd^{3+} 4f moments.³² Previous neutron diffraction studies have shown that the ordering of Nd^{3+} moments occurs below 15 ± 5 K.¹⁰ The temperature-dependent resistivity study shows the absence of a thermally driven metal–insulator transition in the presently investigated $\text{Nd}_2\text{Ir}_2\text{O}_7$ (111) thin film, which is consistent with the earlier study on the polycrystalline $\text{Nd}_2\text{Ir}_2\text{O}_7$ sample.²³ The low temperature (2–55 K) resistivity data signify that the ground state is non-metallic ($d\rho/dT < 0$) in nature²⁵ and probably lies in the semimetallic region.^{27,33} To check the magnetic field (H) induced modification of the charge dynamics, temperature-dependent longitudinal resistivity (ρ_{xx}) measurements were performed under the application of 140 kOe of the magnetic field along [111] direction in both “zero-field cooled” and “field-cooled” conditions. In Fig. 2(b), the green curve corresponds to the measurements in the presence of a 140 kOe field. Although the blue and red curves represent the zero field measurements on trained (ρ_t) and untrained (ρ_{ut}) samples, respectively. Here, trained means that from 300 to 2 K, the sample is cooled under a magnetic field of 140 kOe along the (111) direction and then warmed up in a zero-field. Untrained means the sample is cooled under zero field and then warmed up with no applied field. It is seen that the application of a magnetic field along the [111] direction causes a large reduction of resistivity (green curve) in the low-temperature regime, and the sample becomes more metallic. On the other hand, the trained (ρ_t) and untrained (ρ_{ut}) resistivity show a minimal difference, which corresponds to negligible domain-wall conductance compared to the polycrystal or single crystal samples.^{12,16} This is somewhat expected, as in the present study in the low-temperature region, the bulk AIAO/AOAI AFM domains remain in a semimetallic regime in contrast to the AFM insulating (AFI) ground state of polycrystal or single crystal $\text{Nd}_2\text{Ir}_2\text{O}_7$ samples.^{12,16}

C. Magnetoresistance

A richer perspective on the interaction of the itinerant electrons with the magnetic structure is provided by magnetotransport. Figure 3(a) shows magnetoresistance (MR) data at 2 K for the magnetic fields up to ± 140 kOe applied along the [111] direction. The 2 K MR data show completely negative MR without any sign of saturation up to the highest measured field of 140 kOe. In addition to negative MR, a finite hysteresis between increasing and decreasing field sweeps is also observed. The overall negative MR occurs due to the canting of Ir^{4+} moments along the applied field direction. To properly explain the hysteresis in MR, the whole field sweeping process is described in three different sequences. The green curve (virgin

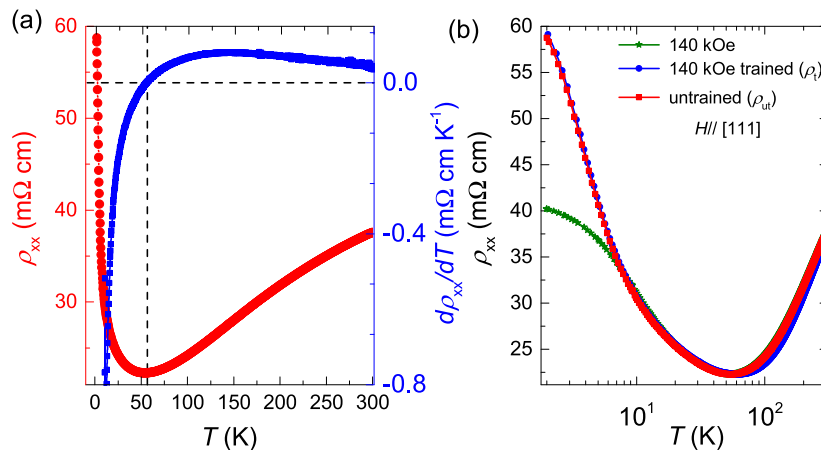


FIG. 2. (a) Temperature dependence of longitudinal resistivity (ρ_{xx}) (red curve) and the corresponding temperature derivative ($d\rho_{xx}/dT$) (blue curve) plot. (b) The green curve corresponds to the temperature dependence of longitudinal resistivity in the presence of 140 kOe applied magnetic fields (H) along the [111] direction. Although the blue and red curves correspond to zero-field longitudinal resistivity measurements on 140 kOe field cooled (ρ_t) and zero field cooled (ρ_{ut}) samples, respectively.

curve) corresponds to sequence 1, in which the field (H) is increased from 0 to the highest measured field of +140 kOe, just after the sample is cooled down to 2 K from 300 K. As the field is increased, the resistivity decreases monotonically, but with a small dip around +34 kOe, above which the resistivity continues to decrease monotonically up to 140 kOe. Note that the dip structure is very similar to the feature observed in a single crystal sample.¹² The virgin loop lies between the subsequent up-and-down sweeps of the hysteresis. In sequence 2 (corresponding to the red curve), field (H) is decreased from +140 to -140 kOe, and a clear dip is observed at -34 kOe. Similarly, in sequence 3 (corresponds to the blue curve), the field (H) is increased from -140 to +140 kOe, and the dip in MR is observed at +34 kOe. The appearance of dip and the presence of hysteresis in MR can be explained by the field-induced plastic domain deformation of Ir^{4+} 5d moments from AOAI (B-domain) to AIAO (A-domain) for the applied positive field and from AIAO (A-domain) to AOAI (B-domain) for the negative field (H), respectively, along the [111] direction.^{12,34} The domain imbalance of Ir^{4+} occurs due to the field-induced modification of the Nd^{3+} spin structure from 4-in-0-out (4I0O) to 1-in-3-out (1I3O) and 4-out-0-in (4O0I) to 1-in-3-out (1I3O), which creates an effective magnetic field (\mathbf{h}_{loc}) at the Ir^{4+} sites through f - d exchange interaction. At $H = 0$, both the A and B domains will be present in equal proportion in the sample.²⁷ In the B-domain, the Ir^{4+} 5d moments will order in the AOAI structure, whereas the Nd^{3+} 4f moments will order in the AIAO structure, as shown in Fig. 3(c). For the A-domain, the spin structure of Ir^{4+} 5d and Nd^{3+} 4f moments will be a time reversal variant of the B-domain. The black dashed hexagon represents the arrangements of the six nearest neighbors Nd^{3+} 4f moments around one Ir^{4+} 5d moment. The effective magnetic field (\mathbf{h}_{loc}) due to the six Nd^{3+} moments at the center of the hexagon will be along the $[\bar{1}\bar{1}\bar{1}]$ direction, i.e., parallel to the central Ir^{4+} moment orientation.

As we increase the field and approach toward +34 kOe, the Zeeman energy of Nd^{3+} moments overcomes the nearest neighbor antiferromagnetic exchange energy, and as a result, the Nd^{3+} spin structure changes from AIAO (4-in-0-out) to 1-in-3-out. The modified spin structure is shown in Fig. 3(d). It is seen that the effective magnetic field at the center of the hexagon (represented by a black dashed line) will change the sign and cause flipping of the Ir^{4+} moment, and consequently, the Ir^{4+} B-domains will be converted into A-domains. It can be seen that the hysteresis is completely closed above +60 kOe, which indicates that +60 kOe of the applied magnetic field along the [111] direction is sufficient enough to convert most of the B-domains into A-domains throughout the sample. A recent single crystal study, along with Monte Carlo simulations for $\text{Ho}_2\text{Ir}_2\text{O}_7$, shows that the A and B domain ratios will be $\sim 70:30$.³⁴ However, in the present case, it may vary as Ho^{3+} and Nd^{3+} have different J_{eff} values. MR data for the temperature range of 3–20 K have been plotted in Fig. 3(b). It can be seen that for 3 K and onwards MR data, the virgin curve is absent, as the field sweeping at 2 K already stabilizes the single domain (majority of A-domain) throughout the sample. The negative MR value decreases as temperature increases, and the hysteresis behavior completely vanishes above 20 K (higher temperature MR data are shown in supplementary material), which is the same as the Nd^{3+} 4f moments ordering temperature.¹⁰ The vanishing of hysteresis in MR above Nd^{3+} ordering temperature indirectly confirms the field-induced modification of Nd^{3+} moments and associated f - d exchange interaction as the underlying mechanism of Ir^{4+} domain switching. It is seen that near zero fields ($H = 0$), the hysteresis loop is closed, indicating that the field sweep rate is slow compared to the magnetic time scale of both the Nd^{3+} and Ir^{4+} moments. Therefore, we are able to explain the observed hysteresis, and the applied [111] field (H) plastically changes the Ir^{4+} domain ratio during the field sweeping process, and f - d exchange interaction plays an important role.

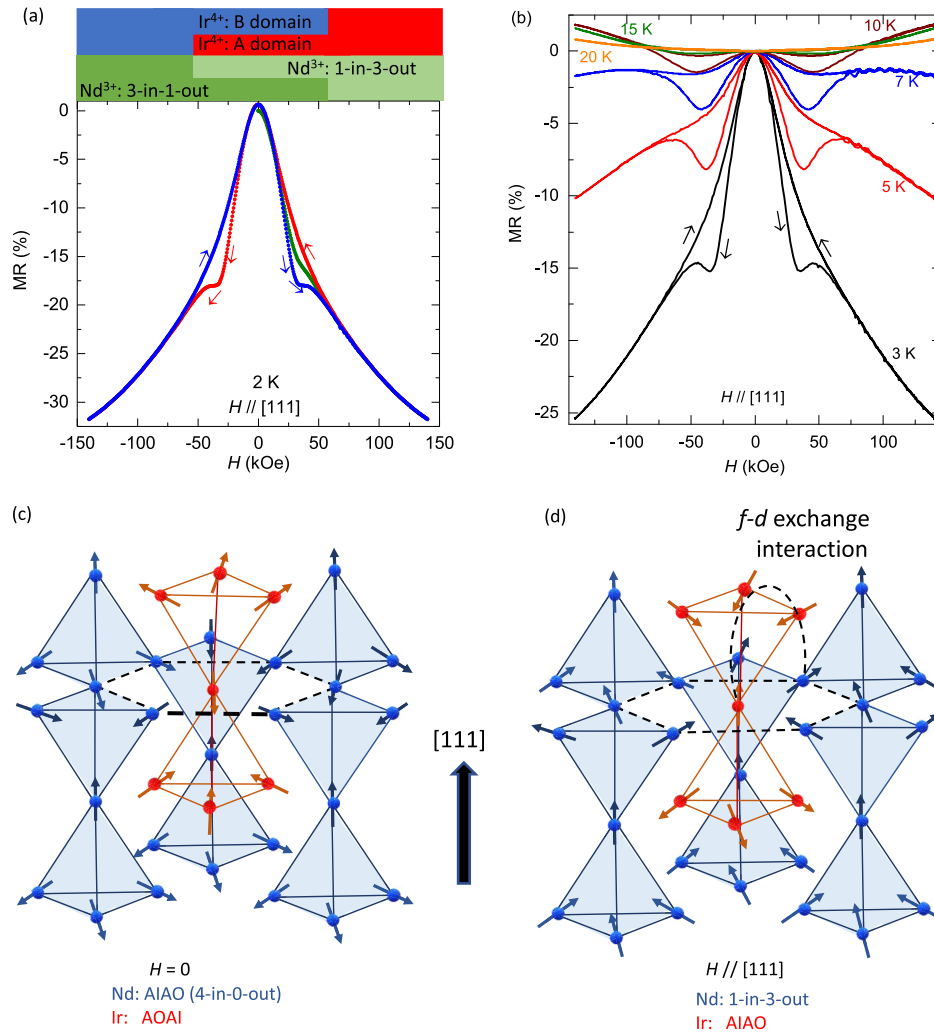


FIG. 3. (a) Magnetic field dependence of the MR plot at 2 K for an [111] applied magnetic field. The possible magnetic structure of $\text{Nd}^{3+} 4f$ (numbers denote spin configuration details, which are discussed in the text) and domain configurations of $\text{Ir}^{4+} 5d$ moments in the strong [111] field limit are shown at the top. (b) MR plot at different fixed temperatures in the range of 3–20 K under an applied magnetic field along the [111] direction. (c) Zero field and low-temperature (below Nd^{3+} ordering temperature) spin structure of $\text{Nd}^{3+} 4f$ moments (blue arrows) having an all-in-all-out ordering and $\text{Ir}^{4+} 5d$ moments (red arrows) with an all-out-all-in order. The black dashed hexagon represents an arrangement of six nearest neighbors $\text{Nd}^{3+} 4f$ moments around one $\text{Ir}^{4+} 5d$ moment. (d) Modified spin structure at sufficiently high [111] magnetic field: the Nd^{3+} moments change the spin structure from 4-in-0-out to 1-in-3-out; consequently, the Ir^{4+} B-domain (AOAI) turns into the A-domain (AIAO) due to the f - d exchange interaction of the modified Nd^{3+} spin structure.

In general, insights into the magnetic domain switching are obtained from the detailed analysis of the antisymmetric part of the hysteretic MR curve.³² The antisymmetric part is defined as

$$\text{MR}^{\text{Asym}}(H) = \frac{\text{MR}(+H) - \text{MR}(-H)}{2}. \quad (1)$$

The antisymmetric part of the 2 K MR data for the field decreasing process (+140 to -140 kOe) is plotted in Fig. 4(a). Antisymmetric behavior will reverse the sign for the field increasing process (-140 to +140 kOe). It is seen that initially, the antisymmetric component increases with field and attains maxima around

~35 kOe, above which, with further increase in field, it decreases and approaches zero at the highest measured field of 140 kOe. In ferromagnetic materials, domain switching occurs at a particular coercive field H_C . However, at finite temperatures and in the presence of unavoidable defects/disorders, the switching process can be broadened. To determine the switching field and account for the broadening, the antisymmetric part of MR(%) (MR^{Asym}) is modeled with an asymmetric Gaussian profile,

$$\text{MR}^{\text{Asym}} = a(e^{-b(H-H_C)^2} - e^{-b(H+H_C)^2}), \quad (2)$$

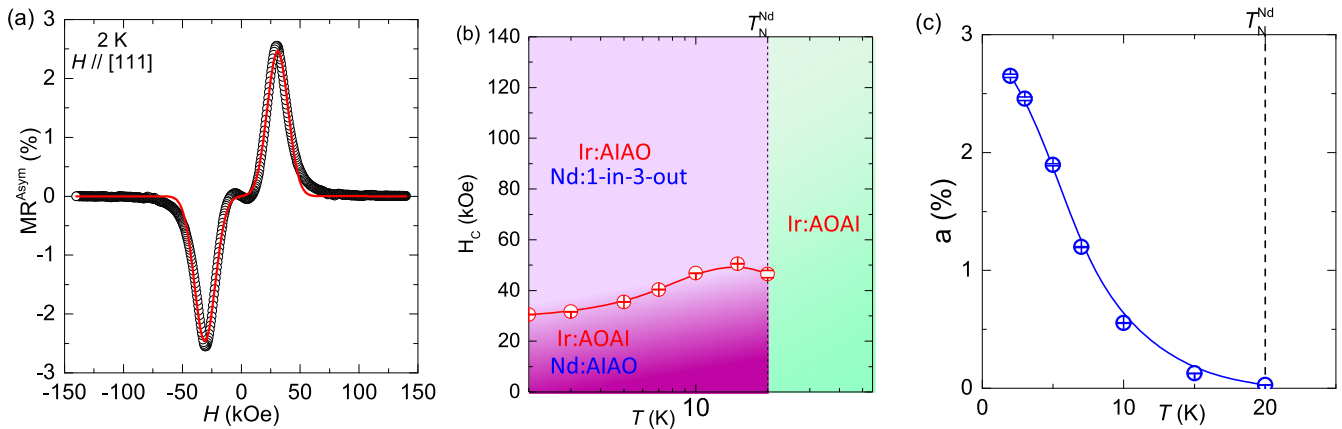


FIG. 4. (a) Antisymmetric part of the 2 K MR data, where the red curve denotes asymmetric Gaussian fitting. (b) Temperature dependence of coercive field (H_C) and the magnetic phase diagram in the plane of magnetic field (H) and temperature (T) along with the corresponding magnetic/spin structure of Nd^{3+} 4f and Ir^{4+} 5d moments. (c) Temperature dependence of the magnitude of the antisymmetric part of the hysteretic MR, where the vertical dashed line guides to the AIAO/AOAI ordering temperature of Nd^{3+} 4f moments.

where a and b are the amplitude and broadening of the hysteresis behavior. The estimated H_C values in the temperature range of 2–20 K are plotted in Fig. 4(b). For the temperature regime of 2–20 K, H_C appears at ~ 35 –45 kOe. For the present case, the majority of the Ir^{4+} domain switching (through the change in the spin structure of Nd^{3+} 4f moments) occurs at the coercive field H_C . Therefore, in the 2–20 K temperature range around H_C , the magnetic structure of Nd^{3+} 4f moments changes from AIAO (4-in-0-out) to 1-in-3-out, and the Ir^{4+} AOAI domain (B-domain) changes to AIAO (A-domain). The corresponding magnetic spin structures of Nd^{3+} and Ir^{4+} in the H – T plane are shown in Fig. 4(b). In order to check how the field-induced domain-imbalance strength varies with temperature, the amplitude (a) of the asymmetric Gaussian function is plotted in Fig. 4(c). It is clearly seen that it decreases with an increase in temperature and vanishes above 20 K (Nd^{3+} ordering temperature).

To check the response of the applied magnetic field (H) along different crystallographic directions, angular dependence of resistivity has been performed at 2 K and 140 kOe of an applied magnetic field. Figure 5(a) shows a schematic of the angle-dependent resistivity. To avoid any contribution from the chiral magnetic effect (angular dependence between current and magnetic field direction), as expected for Weyl semimetals, the magnetic field is always kept perpendicular to the current direction ($I \perp H$), and the sample is rotated about the current (I) axis \parallel $[\bar{1}\bar{1}0]$ direction. Before starting the measurements, a magnetic field of +140 kOe along the $[111]$ direction was applied to realize the AIAO (A-domain) single domain. The angular dependence of resistivity at 2 K has been plotted in Fig. 5(b). $H \parallel [111]$ is defined as the origin ($\theta = 0^\circ$) of the rotation angle. As the field is rotated in the $[111]$ direction, the resistivity increases slowly and reaches a maximum around $\theta = 20^\circ$. As the field rotated further, the resistance decreased monotonically and went through a broad minimum around $\theta = 55^\circ$, which corresponds to the $[001]$ crystallographic axis. Similarly, another broad minimum is observed around $\theta = 137^\circ$ for the field passing

through along the $[\bar{1}\bar{1}0]$ axis and finally reaches the initial value for $\theta = 180^\circ$, corresponding to the $[\bar{1}\bar{1}\bar{1}]$ direction. Therefore, the angle-dependent magnetoresistance measurement shows a highly anisotropic response of the Nd^{3+} and Ir^{4+} moments to the applied magnetic field direction.

For further understanding of the response of Nd^{3+} and Ir^{4+} moments with the applied magnetic field along $[001]$ and $[\bar{1}\bar{1}0]$ directions, we have performed MR measurements at 2 K by applying the magnetic field along those directions, respectively (always keeping $I \perp H$). The corresponding field dependence of MR behavior has been plotted in Figs. 5(c) and 5(d), respectively. The blue and red curves are the MR data for the field (H) increasing and decreasing processes, respectively. The MR data are completely negative up to the highest measured field of ± 140 kOe, and the magnitude of negative MR is larger when compared to that of $[111]$ field direction. The negative MR occurs as the canting of Ir^{4+} moments along the applied field directions causes a reduction in spin-dependent scattering. The MR data for the applied field along $[001]$ direction does not show complete saturation, and there is no order of magnitude change in the resistance as observed in earlier $\text{Nd}_2\text{Ir}_2\text{O}_7$ single crystal studies for an applied field along $[001]$ direction,^{12,13} which indicates the present system (within measurement limits: down to 2 K and up to 140 kOe) is away from the observation of any field-induced quantum phase transition (QPT). The observed QPT in a single crystal study was explained by a reconstruction of the band structure from insulator to nodal line semimetal, associated with the change of magnetic structure of both the Nd^{3+} and Ir^{4+} sublattices from an AIAO/AOAI to 2-in-2-out order. In contrast to the $[111]$ direction, very negligible hysteresis is observed between the up and down sweeps for the applied field along the $[001]$ and $[\bar{1}\bar{1}0]$ axes. This indicates that the application of field (H) up to 140 kOe along the $[001]$ and $[\bar{1}\bar{1}0]$ directions could not plastically modify the domain distribution of Ir^{4+} 5d moments. A recent study by Pearce *et al.* on $\text{Ho}_2\text{Ir}_2\text{O}_7$ also shows the absence of hysteresis in MR for the application of field along the $[001]$ direction.³⁴

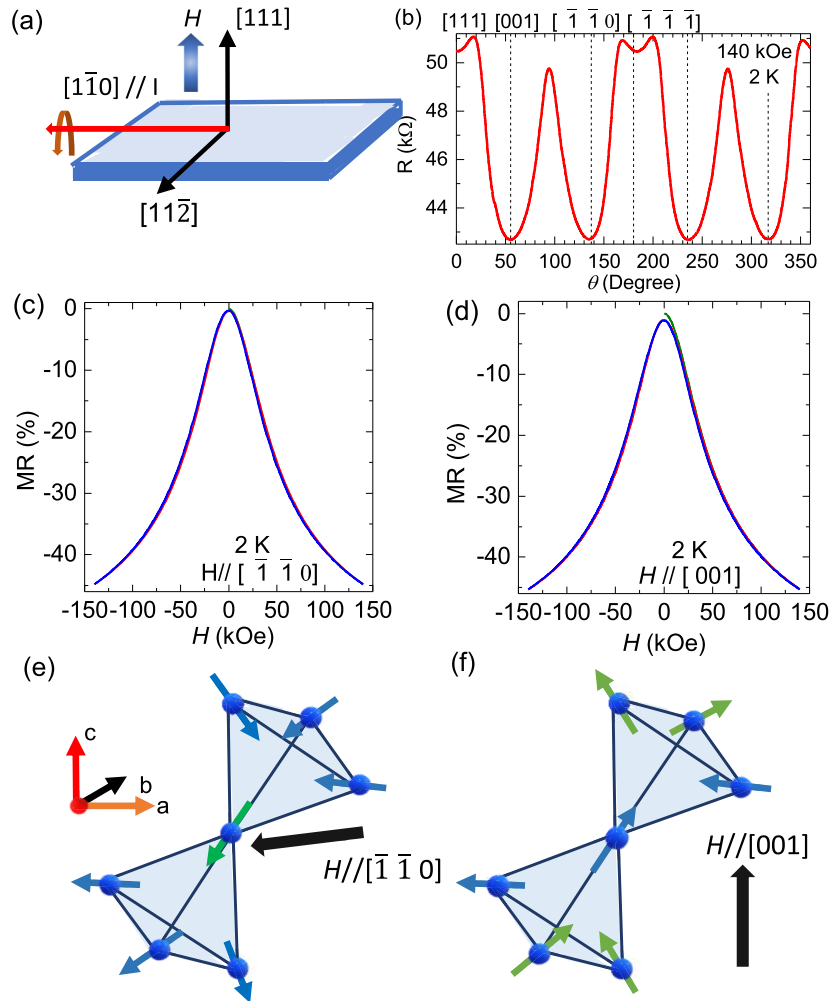


FIG. 5. (a) Schematic diagram of the angle dependence of resistivity measurements. The sample is rotated about the $[1\bar{1}0]$ axis parallel to the current axis such that the magnetic field is always perpendicular to the current. (b) Angle dependence of the resistance plot at 2 K for an applied field of 140 kOe. (c) and (d) MR plot at 2 K for the applied magnetic field along $[1\bar{1}0]$ and $[001]$ directions, respectively; red and blue curves correspond to the field increasing and decreasing processes, whereas the green curve is the virgin curve. Schematic of the modified spin configurations of Nd^{3+} $4f$ moments for an applied field along (e) $[1\bar{1}0]$ and (f) $[001]$ directions, respectively.

The possible modified spin structure of Nd^{3+} $4f$ moments under the application of field along $[1\bar{1}0]$ and $[001]$ directions can be understood by the classical Ising Hamiltonian in the presence of an applied magnetic field and a local magnetic field due to the f - d exchange interaction,

$$\mathcal{H} = -\frac{1}{2}J\sum_{ij} \mathbf{S}_i^{z_i} \cdot \mathbf{S}_j^{z_j} - \sum_i \mathbf{H} \cdot \mathbf{S}_i^{z_i} \pm \sum_i \mathbf{h}_{\text{loc}} \cdot \mathbf{S}_i^{z_i}, \quad (3)$$

for the first term, the summation is over nearest neighbors, \mathbf{H} is the applied magnetic field, $\mathbf{S}_i^{z_i}$ is the moment on the i th atom, which has its own local Ising axis \mathbf{z}_i (local $\langle 111 \rangle$ axis directed toward the center of the tetrahedron), and \mathbf{h}_{loc} is a local field generated at the Nd^{3+} sites due to the nearest six Ir^{4+} moments. In the presence of a field (H),

the magnetic order will be such that there will be a magnetization component along the applied field direction.³⁵

For the applied field (H) along the $[001]$ direction, two spins flip along the $[1\bar{1}1]$ and $[\bar{1}11]$ directions, respectively [shown by green arrows in Fig. 5(f)], to have a positive magnetization component along the applied field direction and from a 2-in-2-out modified spin structure. For the cases of $\text{Ho}_2\text{Ir}_2\text{O}_7$ and $\text{Nd}_2\text{Ir}_2\text{O}_7$ single crystal studies, the application of field along the $[001]$ direction stabilizes the Ho^{3+} and Nd^{3+} moments in a 2-in-2-out configuration, as confirmed by their magnetization measurements along the $[001]$ direction.^{12,34} The modified 2-in-2-out spin configuration of Nd^{3+} $4f$ moments may induce a 2-in-2-out state in Ir^{4+} $5d$ moments via the f - d exchange interaction. Since both the A and B domains of Ir^{4+} $5d$ moments with a 4-in-0-out spin structure will convert to 2-in-2-out ordering, no field-induced plastic domain deformation

will occur for this particular [001] applied field direction. Negligible hysteresis in MR may be due to the field-induced modification in the spin structure of Ir⁴⁺ moments from 4-in-0-out to 2-in-2-out order.

Similarly, for the applied field along the $[\bar{1}\bar{1}0]$ direction, we see that the local axes $[\bar{1}\bar{1}\bar{1}]$ and $[1\bar{1}\bar{1}]$ of the two spins out of the four are perpendicular to the field, so they will not interact with the field.³⁵ Only one spin flips along the $[\bar{1}\bar{1}\bar{1}]$ anisotropy direction with a magnetization component along the applied field direction, shown by the green arrow in Fig. 5(e), which represents the corresponding modified spin structure of Nd³⁺ 4f moments. For the case of Pr₂Ir₂O₇ (111) thin films, the application of an in-plane magnetic field either along the $[1\bar{1}0]$ or $[1\bar{1}\bar{1}]$ directions also shows the absence of hysteresis in the MR curve.³⁶ However, the appearance of hysteresis for the magnetic field along the [011] direction on Ho₂Ir₂O₇ is explained in terms of the high sensitivity of the slight misalignment of the field direction.³⁴

D. Spontaneous Hall effect

To understand the Berry phase contribution of the electronic band structure (presence of Weyl nodes), we have performed Hall measurements for the applied field along $[111]$, $[\bar{1}\bar{1}0]$, and $[001]$ directions, respectively, by keeping the current direction always fixed along $[\bar{1}\bar{1}0]$. The longitudinal MR component (ρ_{xx}) is eliminated by anti-symmetrizing the measured transverse Hall resistivity data. The $[111]$ direction magnetic field (H) dependence of Hall resistivity (ρ_{xy}) at various temperatures in the range of 2–20 K is plotted

in Fig. 6(a). It is seen that for the low temperature (2–5 K) Hall resistivity (ρ_{xy}) data, no linearity in ρ_{xy} is observed even up to the highest measured field of 140 kOe; therefore, we could not subtract the ordinary Hall component ($R_H H$). Furthermore, a large hysteresis ($\sim 75 \mu\Omega \text{cm}$) between up and down field sweeps is observed in the 2 K Hall data. With further increases in temperature, the hysteresis decreases and vanishes above 20 K. Similarly, the 2 K Hall resistivity [$\rho_{xy}(H)$] data for the applied field along $[\bar{1}\bar{1}0]$ and $[001]$ directions are plotted in Figs. 6(b) and 6(c), respectively. These observed Hall effects are unique/unusual compared to the Hall response for the applied field along the $[111]$ direction. A large hysteresis in $\rho_{xy}(H)$ is also observed for these two field directions, but the spontaneous Hall resistivity value $\rho_{xy}(H = 0)$ and coercive field (H_C) vary with the applied field directions. In addition to large hysteresis in the 2 K $\rho_{xy}(H)$ data, a monotonic drop in $\rho_{xy}(H)$ in the high field region is observed for the applied field along $[\bar{1}\bar{1}0]$ and $[001]$ directions but remains almost saturated for the $[111]$ field direction.

For the itinerant ferromagnetic materials, the magnitude of AHE is proportional to the net magnetization (M); $\rho_{xy}^{\text{AHE}}(H) = R_S M$, where M is a measure of macroscopically broken time-reversal symmetry (TRS).^{37,38} However, the AIAO AFM order in Nd₂Ir₂O₇ has negligible spontaneous magnetization ($M \approx 0$, at $H = 0$) (magnetization data are shown in the supplementary material), but microscopic TRS is broken by the AFM order. Therefore, the observed zero field large spontaneous Hall effect (SHE) ($\sim 75 \mu\Omega \text{cm}$) in this TRS broken system cannot be explained by the magnetization-induced origin of AHE. In the earlier Nd₂Ir₂O₇ (111) thin film study by Kim *et al.*, the observed AHE is assigned to the Berry phase origin of the AIAO DWs having broken cubic symmetries.³² However, in the present study, the longitudinal resistivity (ρ_{xx}) measurements on trained and untrained samples show negligible DW conductance. Furthermore, large AHE is also observed for the applied field along $[\bar{1}\bar{1}0]$ and $[001]$ directions [shown in Figs. 6(b) and 6(c)], whereas there is no domain switching or flipping for these particular field directions, as evidenced from the MR measurements [shown in Fig. 5(d)]. Therefore, in the present study, the DW conductance mechanism of the AHE is ruled out. It indicates the presence of some non-trivial momentum space Berry phase curvature ($\Omega(\vec{k})$) origin of the intrinsic AHE. Large Berry phase curvature generally comes from the linear band crossing points or the Weyl nodes. The effects of Berry phase curvature on the AHE will be enhanced if the Weyl points lie at the Fermi level E_F . To get an intrinsic AHC contribution, one needs to integrate the $\Omega(\vec{k})$ of the filled bands over the whole BZ,³⁸

$$\sigma_{xy}^{\text{AHE}} = \frac{e^2}{\hbar} \int_{\text{BZ}} \frac{d^3 \vec{k}}{(2\pi)^3} \sum_n f(\epsilon_n(\vec{k}) - \mu) \Omega_{xy}(\vec{k}), \quad (4)$$

where μ is the chemical potential and $f(\epsilon_n(\vec{k}) - \mu)$ is the Fermi-Dirac distribution function. In Nd₂Ir₂O₇, the proposed WSM with perfect AIAO spin order can host four pairs of Weyl nodes located along the local (111) directions in the BZ.^{18,39} If the proposed WSM phase is stabilized in stoichiometric clean pyrochlore iridates, the Weyl points will lie exactly at the Fermi level.¹ In a perfect cubic lattice, due to the presence of two-fold rotation symmetries C_2 about the x, y, and z axes, $\Omega(\vec{k})$ will be canceled by $\Omega(C_2(\vec{k}))$; as a result, the net contribution of $\Omega(\vec{k})$ to the AHE

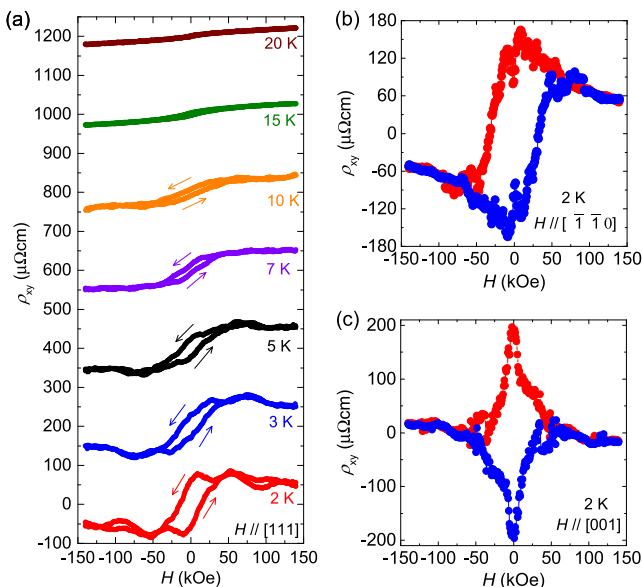


FIG. 6. (a) Magnetic field (H) dependence of the Hall resistivity (ρ_{xy}) plot at different constant temperatures in the range of 2–20 K for the applied field along the $[111]$ direction. The arrows indicate the field-sweeping process. For visual clarity, except for 2 K, the data for different temperatures are shifted vertically. Field variation of the Hall resistivity (ρ_{xy}) at 2 K for the applied field along (b) the $[\bar{1}\bar{1}0]$ and (c) $[001]$ directions, respectively. The red and blue curves correspond to the field decreasing and increasing processes, respectively.

will be hidden. Therefore, the C_2 symmetry needs to be broken to observe an AHE. In the present thin film study, the structural analysis [RSM in Fig. 1(c)] suggests the growth of $\text{Nd}_2\text{Ir}_2\text{O}_7$ on YSZ(111) is most relaxed with cubic symmetry. However, the strain at the film-substrate interface cannot be completely ruled out due to the finite ($\sim 1\%$) lattice mismatch between YSZ and $\text{Nd}_2\text{Ir}_2\text{O}_7$. For epitaxial growth of $\text{Nd}_2\text{Ir}_2\text{O}_7$ thin films on lattice-mismatched YSZ (111) substrate (having both cubic structures), the sample will be under in-plane biaxial compressive strain (as the bulk $\text{Nd}_2\text{Ir}_2\text{O}_7$ lattice parameter is higher than YSZ). Although in the out-of-plane direction, it will be under uniaxial elongated strain. Therefore, the cubic crystal will be stretched along the body diagonal (along the [111] direction) and become a rhombohedral crystal structure, which helps to break the two-fold rotational (C_2) symmetries about the x, y, and z axes. Another recent study on $\sim 1\%$ strained thin films also observed large anomalous Hall conductance and attributed it to the strain-induced electron and hole pocket generation and enhancement of the net Berry curvature effects of the electronic bands.¹⁷ In a recent study on $\text{Sm}_2\text{Ir}_2\text{O}_7$ (111) thin films shows epitaxial strain induced large spontaneous Hall effect.⁴⁰ In the cubic symmetric crystal, if the Ir^{4+} moments are canted by a small angle from the local (111) axis concomitantly, the Weyl points in the BZ will also shift from the $\langle 111 \rangle$ axis and cause non-zero AHE. In the pressure-dependent single crystal (with cubic symmetry) study by Udea *et al.*, the observed SHE signals just below its metal-insulator transition temperature are explained by the small ($\sim 10^{-2}$ rad) spin-canted AIAO spin structure.¹⁸ Therefore, from the above discussion, we infer that the observed large SHE originated from the momentum space Berry curvature and confirmed the presence of Weyl nodes and the predicted WSM phase in $\text{Nd}_2\text{Ir}_2\text{O}_7$.

E. Topological-like Hall component possibly due to the presence of multiple Weyl nodes

In addition to the finite hysteresis, the 2–5 K Hall resistivity $\rho_{xy}(H)$ data in Fig. 6(a) show hump-like features above 50 kOe,

and the strength of the hump increases as the temperature is lowered. A similar hump is also observed in materials having a non-trivial skyrmion-like spin texture^{41,42} and in pyrochlore lattices, $\text{R}_2\text{Mo}_2\text{O}_7$ ($\text{R} = \text{Nd, Sm, Gd}$), $\text{Pr}_2\text{Ir}_2\text{O}_7$ with a non-coplanar spin structure,^{43–48} called the topological Hall effect. However, very recently, the THE-like hall component attained considerable interest and was explained in terms of the multi-component AHE. A few such examples are La-doped EuTiO_3 (001) thin film,⁴⁹ SrRuO_3 (001) thin film,⁵⁰ and magnetic-doped topological insulators.⁵¹ In previous studies by Udea *et al.* on the $\text{Nd}_2\text{Ir}_2\text{O}_7$ single crystal, they also observed multiple Weyl node induced complex Hall effects.^{18,39} Therefore, to explain all the observed complex features, the 3 K Hall resistivity data are expressed as a combination of hysteretic and non-hysteretic components. In Fig. 7(a), the red curve is the measured Hall resistivity at 3 K, whereas the black curve is the fitted data, which is a sum of the hysteretic and the non-hysteretic components. The hysteretic part of the Hall resistivity is shown by the red curve in Fig. 7(b), which can be expressed by a sum of two curves, green and blue, as shown in Fig. 7(b). The green and blue curves have opposite field dependence and are called a hysteresis (green curve) and an anti-hysteresis (blue curve). Here, we have tried to capture both the hysteretic/anti-hysteretic AHE components by using an empirical hysteretic tangent hyperbolic function,

$$\rho_{xy}^{\text{AHE}}(H) = \pm a_{\text{Ir}} \tanh [b_{\text{Ir}}(H \pm H_C)], \tag{5}$$

where a_{Ir} , b_{Ir} , and H_C are the amplitude, zero-field slope, and coercive field, respectively, the values of which are chosen to ensure a good capture of the hysteresis part of the experimental AHE signal. Here, we have tried to capture the individual AHE components in terms of the tanh function because the higher temperature Hall data, where only a single component of AHE is present, can be nicely captured by the hysteretic tanh (sigmoidal) function. Although the non-hysteretic part of the Hall resistivity is shown by the red curve

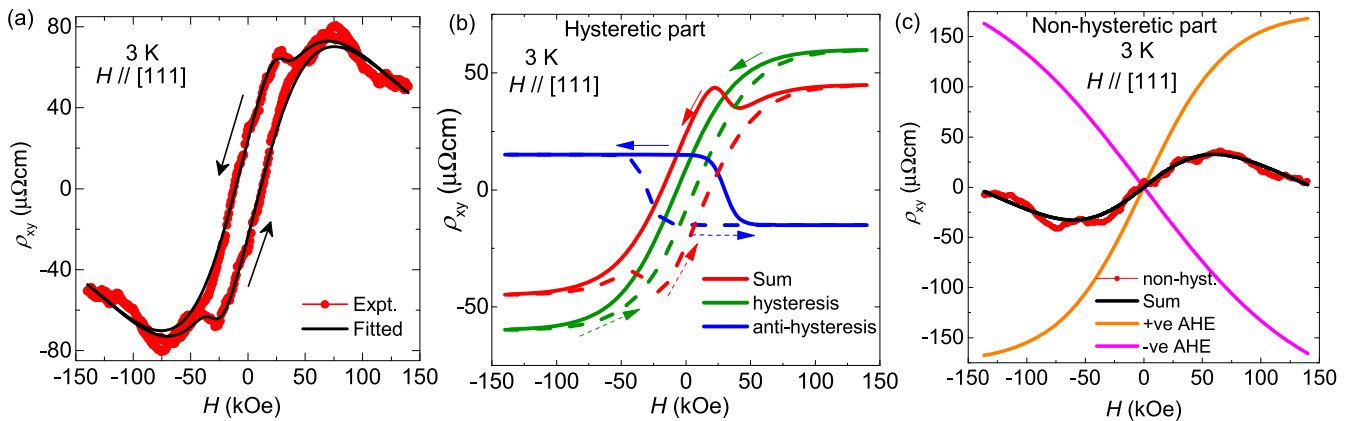


FIG. 7. (a) Magnetic field-dependence of Hall resistivity [$\rho_{xy}(H)$] at 3 K, where both the anomalous and topological-like Hall components are present, the black fitted curves are a resultant of four different Hall components (hysteretic as well as non-hysteretic). (b) The red curve corresponds to the hysteretic part of the Hall resistivity at 3 K, which can be represented by a sum of the hysteretic (green curve) and anti-hysteretic (blue-curve) AHE curves. (c) The red curve represents the non-hysteretic THE-like Hall component of 3 K Hall data (obtained after subtracting the simulated AHE from the measured Hall data), which can be represented by a sum (by the black curve) of the +ve (orange curve) and -ve (magenta curve) AHE components.

in Fig. 7(c). Similar to the hysteretic part, the non-hysteretic part can also be represented by a sum of the two separate non-hysteretic AHE components (the non-hysteretic tangent hyperbolic function), shown by the orange and magenta curves, respectively, and named as +ve and -ve AHE, respectively. The black curve represents the sum of the +ve and -ve AHE, which nicely matches the non-hysteretic part (red curve). Both the hysteretic and non-hysteretic AHEs have a non-trivial momentum space Berry curvature $[\Omega(\vec{k})]$ induced origin. This appearance of hysteretic and anti-hysteretic, as well as +ve and -ve AHE, is most likely determined by the position of band-crossing points or Weyl points relative to the Fermi level. Since, we could explain the observed/measured Hall resistivity in terms of the four Hall components, it can be thought that the electronic band structure of the material has different types of sources of Berry curvatures $[\Omega(\vec{k})]$. Therefore, the topological-like Hall effect (or multi-component AHE) in $\text{Nd}_2\text{Ir}_2\text{O}_7$ (111) thin film most likely arises due to the presence of multiple Weyl nodes in the electronic band structure. Therefore, our detailed analysis of the AHE suggests the possibility of the presence of multiple Weyl nodes near the Fermi level. Different Weyl nodes might have different responses to the applied magnetic field and can generate different AHE components.

Similarly, the observed unique/unusual Hall effect for the applied field along $[\bar{1}\bar{1}0]$ and $[001]$ directions might also arise due to the presence of multiple Weyl nodes. Since the response of the Weyl points will be different for the different applied field directions, the measured Hall data show different behavior. However, to completely capture all the features in the Hall data for the applied field along $[\bar{1}\bar{1}0]$ or $[001]$ directions, a detailed theoretical calculation is highly desirable. Therefore, observation of the THE-like Hall effects suggests the possibility of the presence of multiple Weyl nodes near the Fermi level. Different Weyl nodes might have different responses to the applied magnetic field and can generate different AHE components.

IV. CONCLUSION

In the present thin film study, we have observed negligible domain wall (DW) conductance between AIAO/AOAI AFM domains. Temperature-dependent longitudinal resistivity (ρ_{xx}) measurement shows the absence of the metal-insulator transition and a semimetallic AFM ground state. Magnetotransport measurements show a highly anisotropic magnetoresistance of both the Nd^{3+} 4*f* and Ir^{4+} 5*d* moments. Application of magnetic field (*H*) along $[111]$ direction causes a field-induced plastic imbalance of Ir^{4+} AIOA/AOAI domains, which results from the change of Nd^{3+} 4*f* moments spin order from 4-in-0-out to 1-in-3-out and the associated *f-d* exchange interaction. This field-induced domain imbalance causes large hysteresis in MR. However, applying the field along the $[001]$ and $[\bar{1}\bar{1}0]$ directions does not cause any domain imbalance. Hall resistivity $[\rho_{xy}(H)]$ data show the appearance of a large intrinsic (momentum space Berry phase induced) spontaneous Hall effect, which signifies the presence of Weyl points in the electronic band structure. Furthermore, a THE-like Hall component arises, possibly due to the presence of multiple Weyl nodes in the electronic band structure. This study shows that $\text{Nd}_2\text{Ir}_2\text{O}_7$ (111) thin films offer a fertile ground state for observing novel

phenomena induced by strong geometrical and magnetic frustration and non-trivial electronic band-topology.

SUPPLEMENTARY MATERIAL

See the supplementary material for the details of the atomically flat YSZ (111) substrate preparation, magnetization data and higher-temperature magnetoresistance data.

ACKNOWLEDGMENTS

MG would like to acknowledge the MoE, India, for financial support. PSAK acknowledges IRPHA and DST, India, for funding support.

AUTHOR DECLARATIONS

Conflict of Interest

The authors have no conflicts to disclose.

Author Contributions

Mithun Ghosh: Conceptualization (equal); Data curation (lead); Formal analysis (lead); Investigation (equal); Methodology (equal); Writing – original draft (lead). **P. D. Babu:** Data curation (equal); Resources (equal); Supervision (equal); Writing – review & editing (equal). **P. S. Anil Kumar:** Conceptualization (equal); Funding acquisition (lead); Methodology (equal); Project administration (lead); Resources (lead); Supervision (lead); Writing – review & editing (lead).

DATA AVAILABILITY

The data that support the findings of this study are available from the corresponding author upon reasonable request.

REFERENCES

- X. Wan, A. M. Turner, A. Vishwanath, and S. Y. Savrasov, *Phys. Rev. B* **83**, 205101 (2011).
- W. Witczak-Krempa and Y. B. Kim, *Phys. Rev. B* **85**, 045124 (2012).
- S. Lee, A. Paramakanti, and Y. B. Kim, *Phys. Rev. Lett.* **111**, 196601 (2013).
- Y. Yamaji and M. Imada, *Phys. Rev. X* **4**, 021035 (2014).
- J. S. Gardner, M. J. P. Gingras, and J. E. Greedan, *Rev. Mod. Phys.* **82**, 53 (2010).
- Y. Wang, H. Weng, L. Fu, and X. Dai, *Phys. Rev. Lett.* **119**, 187203 (2017).
- K. Matsuhira, M. Wakeshima, Y. Hinatsu, and S. Takagi, *J. Phys. Soc. Jpn.* **80**, 094701 (2011).
- K. Matsuhira, M. Wakeshima, R. Nakanishi, T. Yamada, A. Nakamura, W. Kawano, S. Takagi, and Y. Hinatsu, *J. Phys. Soc. Jpn.* **76**, 043706 (2007).
- H. Guo, C. Ritter, and A. C. Komarek, *Phys. Rev. B* **94**, 161102 (2016).
- K. Tomiyasu, K. Matsuhira, K. Iwasa, M. Watahiki, S. Takagi, M. Wakeshima, Y. Hinatsu, M. Yokoyama, K. Ohoyama, and K. Yamada, *J. Phys. Soc. Jpn.* **81**, 034709 (2012).
- G. Chen and M. Hermele, *Phys. Rev. B* **86**, 235129 (2012).
- K. Ueda, J. Fujioka, B. J. Yang, J. Shiozai, A. Tsukazaki, S. Nakamura, S. Awaji, N. Nagaosa, and Y. Tokura, *Phys. Rev. Lett.* **115**, 056402 (2015).

- ¹³Z. Tian, Y. Kohama, T. Tomita, H. Ishizuka, T. Hsieh, J. J. Ishikawa, K. Kindo, L. Balents, and S. Nakatsuji, *Nat. Phys.* **12**, 134–138 (2016).
- ¹⁴I. Kapon, C. W. Rischau, B. Michon, K. Wang, B. Xu, Q. Yang, S. Nakatsuji, and D. Van Der Marel, *Phys. Rev. Res.* **4**, 023056 (2022).
- ¹⁵S. M. Disseler, S. R. Giblin, C. Dhital, K. C. Lukas, S. D. Wilson, and M. J. Graf, *Phys. Rev. B* **87**, 060403 (2013).
- ¹⁶K. Matsuhira, M. Tokunaga, M. Wakeshima, Y. Hinatsu, and S. Takagi, *J. Phys. Soc. Jpn.* **82**, 023706 (2013).
- ¹⁷W. J. Kim, T. Oh, J. Song, E. K. Ko, Y. Li, J. Mun, B. Kim, J. Son, Z. Yang, Y. Kohama *et al.*, *Sci. Adv.* **6**, eabb1539 (2020).
- ¹⁸K. Ueda, R. Kaneko, H. Ishizuka, J. Fujioka, N. Nagaosa, and Y. Tokura, *Nat. Commun.* **9**, 3032 (2018).
- ¹⁹K. Ueda, J. Fujioka, Y. Takahashi, T. Suzuki, S. Ishiwata, Y. Taguchi, M. Kawasaki, and Y. Tokura, *Phys. Rev. B* **89**, 075127 (2014).
- ²⁰E. Y. Ma, Y. T. Cui, K. Ueda, S. Tang, K. Chen, N. Tamura, P. M. Wu, J. Fujioka, Y. Tokura, and Z. X. Shen, *Science* **350**, 538–541 (2015).
- ²¹K. Ueda, J. Fujioka, Y. Takahashi, T. Suzuki, S. Ishiwata, Y. Taguchi, and Y. Tokura, *Phys. Rev. Lett.* **109**, 136402 (2012).
- ²²K. Ueda, J. Fujioka, and Y. Tokura, *Phys. Rev. B* **93**, 245120 (2016).
- ²³S. M. Disseler, C. Dhital, T. C. Hogan *et al.*, *Phys. Rev. B* **85**, 174441 (2012).
- ²⁴D. Yanagishima and Y. Maeno, *J. Phys. Soc. Jpn.* **70**, 2880–2883 (2001).
- ²⁵J. J. Ishikawa, E. C. T. O’Farrell, and S. Nakatsuji, *Phys. Rev. B* **85**, 245109 (2012).
- ²⁶M. Nakayama, T. Kondo, Z. Tian, J. J. Ishikawa, M. Halim, C. Bareille, W. Malaeb, K. Kuroda, T. Tomita, S. Ideta *et al.*, *Phys. Rev. Lett.* **117**, 056403 (2016).
- ²⁷M. Ghosh, S. G. Bhat, A. Pal, and P. S. A. Kumar, *J. Phys.: Condens. Matter* **34**, 165701 (2022).
- ²⁸K. Y. Yang, Y. M. Lu, and Y. Ran, *Phys. Rev. B* **84**, 075129 (2011).
- ²⁹B. J. Yang and N. Nagaosa, *Phys. Rev. Lett.* **112**, 246402 (2014).
- ³⁰T. Honke, H. Fujioka, J. Ohta, and M. Oshima, *J. Vac. Sci. Technol., A* **22**, 2487 (2004).
- ³¹H. Guo, K. Matsuhira, I. Kawasaki, M. Wakeshima, Y. Hinatsu, I. Watanabe, and Z. Xu, *Phys. Rev. B* **88**, 060411 (2013).
- ³²W. J. Kim, J. H. Gruenewald, T. Oh, S. Cheon, B. Kim, O. B. Korneta, H. Cho, D. Lee, Y. Kim, M. Kim *et al.*, *Phys. Rev. B* **98**, 125103 (2018).
- ³³M. Ghosh, D. Samal, and P. S. Anil Kumar, *Phys. Rev. B* **106**, 085139 (2022).
- ³⁴M. J. Pearce, K. Gotze, A. Szabo, T. S. Sikkenk, M. R. Lees, A. T. Boothroyd, D. Prabhakaran, C. Castelnovo, and P. A. Goddard, *Nat. Commun.* **13**, 444 (2022).
- ³⁵M. J. Harris, S. T. Bramwell, P. C. W. Holdsworth, and J. D. M. Champion, *Phys. Rev. Lett.* **81**, 4496 (1998).
- ³⁶Y. Li, T. Oh, J. Son, J. Song, M. K. Kim, D. Song, S. Kim, S. H. Chang, C. Kim, B. J. Yang, and T. W. Noh, *Adv. Matter.* **33**, 2008528 (2021).
- ³⁷N. Nagaosa, J. Sinova, S. Onoda, A. H. MacDonald, and N. P. Ong, *Rev. Mod. Phys.* **82**, 1539 (2010).
- ³⁸M. Onoda and N. Nagaosa, *J. Phys. Soc. Jpn.* **71**, 19–22 (2002).
- ³⁹K. Ueda, T. Oh, B. J. Yang, R. Kaneko, J. Fujioka, N. Nagaosa, and Y. Tokura, *Nat. Commun.* **8**, 15515 (2017).
- ⁴⁰M. Ghosh and P. S. A. Kumar, *Phys. Rev. B* **108**, 075145 (2023).
- ⁴¹A. Neubauer, C. Pfleiderer, B. Binz, A. Rosch, R. Ritz, P. G. Niklowitz, and P. Boni, *Phys. Rev. Lett.* **102**, 186602 (2009).
- ⁴²Y. Fujishiro, N. Kanazawa, T. Nakajima, X. Z. Yu, K. Ohishi, Y. Kawamura, K. Kakurai, T. Arima, H. Mitamura, A. Miyake *et al.*, *Nat. Commun.* **10**, 1059 (2019).
- ⁴³Y. Taguchi, T. Sasaki, S. Awaji, Y. Iwasa, T. Tayama, T. Sakakibara, S. Iguchi, T. Ito, and Y. Tokura, *Phys. Rev. Lett.* **90**, 257202 (2003).
- ⁴⁴Y. Taguchi, Y. Oohara, H. Yoshizawa, N. Nagaosa, and Y. Tokura, *Science* **291**, 2573–2576 (2001).
- ⁴⁵Y. Machida, S. Nakatsuji, Y. Maeno, T. Tayama, T. Sakakibara, and S. Onoda, *Phys. Rev. Lett.* **98**, 057203 (2007).
- ⁴⁶M. Udagawa and R. Moessner, *Phys. Rev. Lett.* **111**, 036602 (2013).
- ⁴⁷Y. Taguchi and Y. Tokura, *Phys. Rev. B* **60**, 10280 (1999).
- ⁴⁸T. Katsufuji, H. Y. Hwang, and S. W. Cheong, *Phys. Rev. Lett.* **84**, 1998 (2000).
- ⁴⁹K. S. Takahashi, H. Ishizuka, T. Murata, Q. Y. Wang, Y. Tokura, N. Nagaosa, and M. Kawasaki, *Sci. Adv.* **4**, eaar7880 (2018).
- ⁵⁰G. Kimbell, P. M. Sass, B. Woltjes, E. K. Ko, T. W. Noh, W. Wu, and J. W. A. Robinson, *Phys. Rev. Mater.* **4**, 054414 (2020).
- ⁵¹K. M. Fijalkowski, M. Hartl, M. Winnerlein, P. Mandal, S. Schreyeck, K. Brunner, C. Gould, and L. W. Molenkamp, *Phys. Rev. X* **10**, 011012 (2020).